

NANO-STRUCTURED VERMICULITE CLAY FOR HIGH-PERFORMANCE ADSORPTION OF MALACHITE GREEN DYE: STRUCTURAL CHARACTERIZATION AND REGENERATION POTENTIAL

Aseel M. Aljeboree^{1,*}, Ali Fawzi Al-Hussainy², Usama S. Altimari³, Shaima Abd⁴,
Zainab A. Alhassan⁵, Ayad F. Alkaim¹

¹Department of Chemistry, College of Sciences for Girls, University of Babylon, Hilla, Iraq

²College of Pharmacy / Ahl Al Bayt University / Kerbala / Iraq

³AL-Nisour University College, Department of Medical Laboratories Technology, Baghdad, Iraq

⁴Department of Sciences/ Al-Manara College For Medical Sciences/ (Maysan)/Iraq

⁵Mazaya University College, Department of Medical Laboratories Technology, Iraq

*e-mail: annenayad@gmail.com

Received 10.05.2025

Accepted 27.07.2025

Abstract: This study employed nanoclay as a low-cost, environmentally friendly adsorbent for the effective removal of malachite green (MG) dye from aqueous solutions. The nanoclay was characterized using XRD, FESEM, TEM, TGA, and FTIR. Structural and morphological analyses confirmed a porous, multilayered structure that was enhanced after adsorption. Batch experiments were conducted to evaluate the impact of key parameters, including dye concentration (10–100 mg/L), adsorbent dosage (0.02–0.15 g), contact time (5–60 min), temperature (10–40 °C), and pH (2–11). Adsorption equilibrium was reached within 60 minutes, and the highest removal efficiency (92.84%) was achieved under optimal conditions: 0.1 g of adsorbent, pH 7, 80 mg/L dye concentration, 60 minutes of contact time, and 30 °C. FTIR analysis confirmed the interaction of MG dye with hydroxyl and Si–O–Si functional groups through observed spectral shifts. FESEM and TEM images revealed increased surface porosity and dye–particle interaction. XRD analysis confirmed the crystalline nature of the nanoclay and minimal structural disruption after adsorption. Isotherm studies showed that the adsorption process followed the Freundlich model, indicating heterogeneous surface adsorption. Kinetic modelling revealed that the data fitted well with the pseudo-second-order model, suggesting chemisorption as the dominant mechanism. Thermodynamic parameters (ΔG° , ΔH° , and ΔS°) indicated that the adsorption was spontaneous and exothermic. Regeneration tests over five cycles using ethanol and distilled water demonstrated that nanoclay retained over 90% of its initial efficiency, confirming its excellent reusability and structural stability. Overall, nanoclay proved to be a promising and sustainable adsorbent for treating dye-contaminated wastewater.

Keyword: Vermiculite, Clay, Dye, Malachite green, Nano, Removal, Regeneration

Introduction

Recently, clay minerals have attracted widespread interest in environmental remediation due to their abundance, low cost, high surface area, and ion-exchange capacity. These naturally occurring layered silicates exhibit unique physical and chemical properties, making them effective adsorbents for various pollutants, particularly organic, inorganic, and synthetic dyes commonly found in industrial wastewater. Among the different types of clay, vermiculite stands out for its superior cation-exchange capacity, thermal stability, and structural flexibility [1, 2].

Vermiculite is a clay mineral composed of hydrated magnesium-aluminum-iron silicates, characterized by a 2:1 layered structure, with an octahedral sheet sandwiched between two tetrahedral sheets. Upon heating, vermiculite expands significantly due to the evaporation of water between the layers, increasing its surface area and enhancing its adsorption capacity. This clay has a high affinity for cationic dyes due to its negatively charged layers and large interlayer spacing, facilitating electrostatic interactions and cross-linking processes [3, 4]. In recent years, vermiculite has been explored as an environmentally friendly and renewable adsorbent for removing hazardous dyes from aqueous media, such as methyl violet, malachite green, and methylene blue. Its structural properties enable efficient adsorption through ion exchange, hydrogen bonding, and the formation

of surfactants. Furthermore, the potential to reuse vermiculite through regeneration treatments supports its application in sustainable wastewater treatment technologies [5].

Environmental pollution, especially water pollution, has become a significant global issue due to the increasing discharge of industrial wastewater into aquatic ecosystems. Among the various pollutants, synthetic dyes used in the textile, paper, leather, and plastics industries substantially threaten water quality and public health. These dyes are often toxic, non-biodegradable, and resistant to conventional wastewater treatment processes, resulting in their environmental accumulation [3, 6]. This accumulation hurts both aquatic life and human health. One such dye, malachite green (MG) (Fig. 1), is a cationic triphenylmethane dye widely used in dyeing silk, wool, and leather, as well as in aquaculture for its antifungal and antiparasitic properties. Malachite green is highly toxic, carcinogenic, and mutagenic despite its effectiveness. Its persistence in water bodies can lead to severe ecological imbalances and bioaccumulation in aquatic organisms. Given its hazardous nature, removing malachite green from wastewater has become a priority in environmental research. Several advanced treatment techniques, including adsorption, photocatalysis, and membrane filtration, have been employed to remove malachite green from aqueous solutions. Among these methods, adsorption using low-cost natural or modified adsorbents has garnered significant attention due to its simplicity, efficiency, and economic feasibility [7-9].

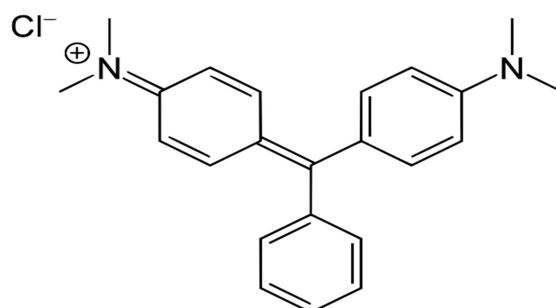


Fig. 1. Chemical structure of malachite green (MG)

Experimental part

Adsorption study. The stock solution of MG dye was diluted to the desired concentrations to prepare a standard dye solution, ranging from 10 to 100 mg/L. For batch mode adsorption tests, 100 mL conical flasks were filled with 0.1 g of adsorbent and 100 mL of the prepared dye solution, maintaining an initial pH of 7. Using a mechanical shaker, the flasks were shaken at 120 rpm for 1 hour at a temperature of $25 \pm 2^\circ\text{C}$. After agitation, centrifugation was performed to separate the adsorbent from the adsorbate. The dye content in the supernatant was then measured using spectrophotometry at a wavelength of 625 nm.

Experiments were conducted at a constant dye concentration of 80 mg/L, with varying clay dosages ranging from 0.03 to 0.15 g per 100 mL, to investigate the effect of clay dosage on the percentage of dye elimination. Additionally, the impact of dye concentration on the elimination percentage was studied, with concentrations ranging from 10 to 100 mg/L, while maintaining a consistent adsorbent dosage of 0.1 g per 100 mL. The amount of adsorption at equilibrium was calculated using the appropriate formula.

$$\text{removal efficiency \%} = \frac{C_0 - C_e}{C_0} \times 100 \quad (1)$$

$$\text{adsorption capacity} = \frac{(C_0 - C_e)V}{m(\text{g})} \quad (2)$$

where C_0 (mg/L) is the initial concentration of dye, C_e (mg/L) is the concentration of MG dye at equilibrium, V (mL) is the volume of the solution, and m (g) is the weight of the clay.

Results and discussion

FE-SEM. Field-emission scanning electron microscopy (FE-SEM), as shown in Fig. 2, was used to examine the morphological properties of the clay before and after adsorption. This high-resolution imaging technique offers comprehensive insights into surface topography, particle shape, degree of agglomeration, and textural properties, including surface smoothness, porosity, and homogeneity of particle distribution. The FE-SEM image of the raw clay (Fig. 2a) shows a relatively smooth and compact surface morphology with limited visible porosity. The clay particles appear densely packed, with lamellar-like structures and minimal surface irregularities, indicating a low specific surface area and limited exposure of active adsorption sites. This suggests that the clay exhibits a relatively organized structure before adsorption with poor surface contrast. After adsorption (Fig. 2b), significant morphological transformations are observed. The clay surface becomes rougher and irregular, characterized by the appearance of a sponge-like porous network. Numerous micro- and medium-sized pores appear on the surface, forming randomly oriented wrinkles and folds. These structural changes indicate an increase in surface area and porosity, likely resulting from the interaction between the adsorbent molecules and the clay matrix. Furthermore, the agglomeration of the clay layers appears more pronounced, possibly due to the swelling of the interlayers and the formation of van der Waals interactions and hydrogen bonds between the adsorbent molecules and the clay surface. These observations confirm the effectiveness of the adsorption process and the significant reorganization of the clay surface structure [10, 11].

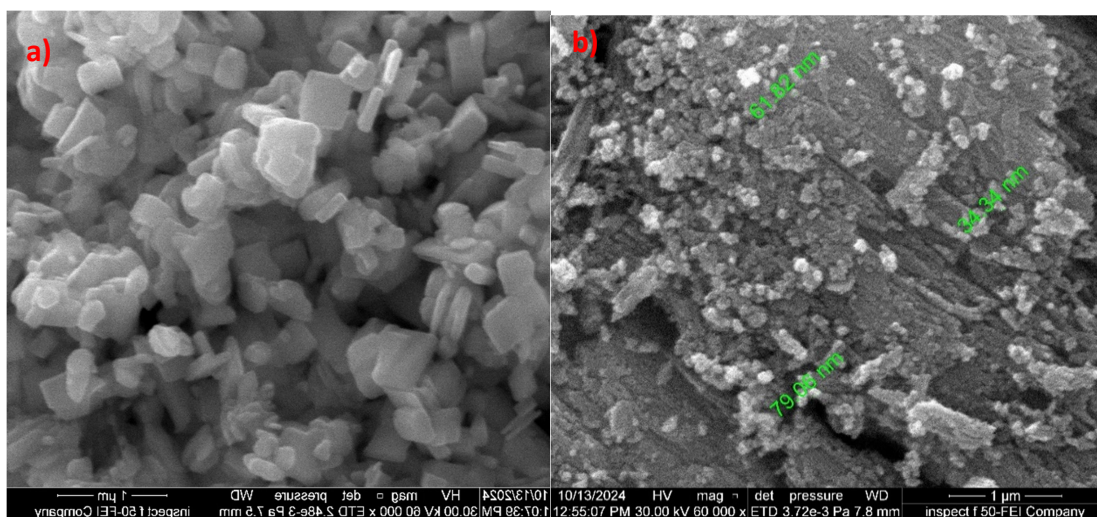


Fig. 2. Field-emission scanning electron microscopy (FE-SEM) (a) Clay, (b) Clay-MG dye

TEM. *Structure, shape, and particle dispersion at the nanoscale.* As shown in Fig. 3, the transmission electron microscope image shows clay particles distributed against a bright, contrasting background, clearly visualizing their shape and spatial arrangement. The observed clay particles appear darker in color due to their high electron density compared to the background. These particles exhibit a spherical to irregular shape, with an average particle diameter of approximately 60 nm. The particles are relatively well distributed across the field of view, indicating moderate homogeneity in distribution. However, areas of slight agglomeration are also evident, where particles form denser clusters of varying sizes [12]. These agglomerated areas appear as dark patches, indicating localized interactions between particles. This partial agglomeration is likely due to van der Waals forces or incomplete exfoliation of the clay layers during sample preparation. Despite the slight agglomeration, the overall dispersion remains acceptable, supporting the effectiveness of the clay consolidation process. The image also highlights the nanoscale dimensions of the particles, which enhances their surface-to-volume ratio and indicates a high potential for interaction with adsorbent molecules [13].

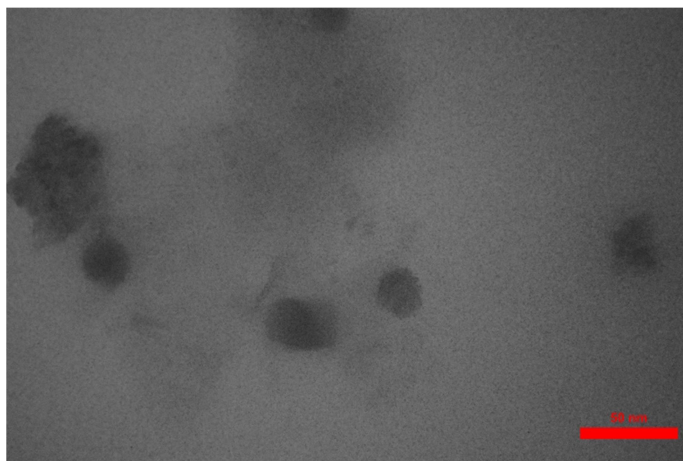


Fig. 3. Transmission electron microscope image of clay

X-ray diffraction (XRD). X-ray diffraction (XRD) analysis is fundamental for studying crystal structure, interlayer spacing, and phase composition of clay materials. In this study, X-ray diffraction patterns of clay sorbents were recorded over a 2θ range of $10\text{--}80^\circ$, providing a deeper understanding of the degree of crystallinity and the nature of the mineral phases. As shown in Fig. 4, the diffraction pattern exhibits distinct peaks at 2θ values of 28.18° , 35.91° , 38.53° , and 45.04° [14]. The appearance and intensity of these peaks indicate a high degree of crystallinity, consistent with well-ordered atomic planes within the clay structure. Compared to standard reference patterns, the observed shift in peak positions may be attributed to structural modifications resulting from interactions with adsorbents, ion exchange processes, or changes in interlayer spacing. These diffraction peaks correspond to specific crystal planes, indicating the presence of layered silicate minerals with distinct basal spacing. These structural features play a critical role in the clay's adsorption capacity, affecting the accessibility of active sites and the total surface area. The presence of sharp, well-defined peaks confirms that the clay retains its crystalline integrity after treatment and supports its potential as an effective adsorbent [15, 16].

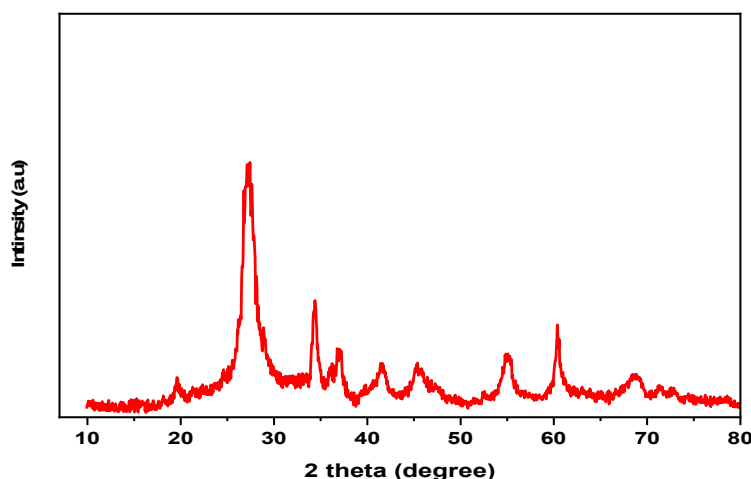


Fig. 4. X-ray diffraction (XRD) analysis of Vermiculite Clay

Fourier Transform Infrared Spectroscopy (FTIR). Fourier Transform Infrared Spectroscopy (FTIR) was employed to investigate the functional groups in the clay surface before and after the adsorption process, as illustrated in Fig. 5. The FTIR spectra provide valuable information regarding the chemical bonds and molecular vibrations associated with the clay's surface functionalities. In the spectrum recorded for raw clay, a broad absorption band is observed within the range of $2500\text{--}3500\text{ cm}^{-1}$. This broad feature is primarily attributed to overlapping vibrational modes, including O–H stretching vibrations from hydroxyl groups (–OH) and carboxylic

acid ($-\text{COOH}$) groups. The breadth of this band suggests the presence of hydrogen bonding, commonly associated with structural $-\text{OH}$ groups and adsorbed water molecules on the clay surface. A notable peak of vigorous intensity appears around 980 cm^{-1} , corresponding to the asymmetric stretching vibration of the $\text{Si}-\text{O}-\text{Si}$ bond. This peak is characteristic of silicate frameworks and indicates the presence of well-defined silicate structures within the clay matrix [17].

Additionally, the absorption region spanning $3300\text{--}2500\text{ cm}^{-1}$ may include contributions from the stretching vibrations of $\text{C}=\text{O}$ bonds (carbonyl groups), which can originate from organic matter or surface functionalization. Peaks near 3500 cm^{-1} are typically linked to the stretching vibrations of free hydroxyl groups ($-\text{OH}$) and physically adsorbed water (H_2O), further confirming the hydrophilic nature of the clay surface. After the adsorption process, noticeable changes occur in the intensity and position of several bands, suggesting successful interaction between the clay surface and the adsorbed species. These spectral shifts reflect modifications in surface chemistry, such as hydrogen bonding, complexation, or the incorporation of functional groups from the adsorbate [18].

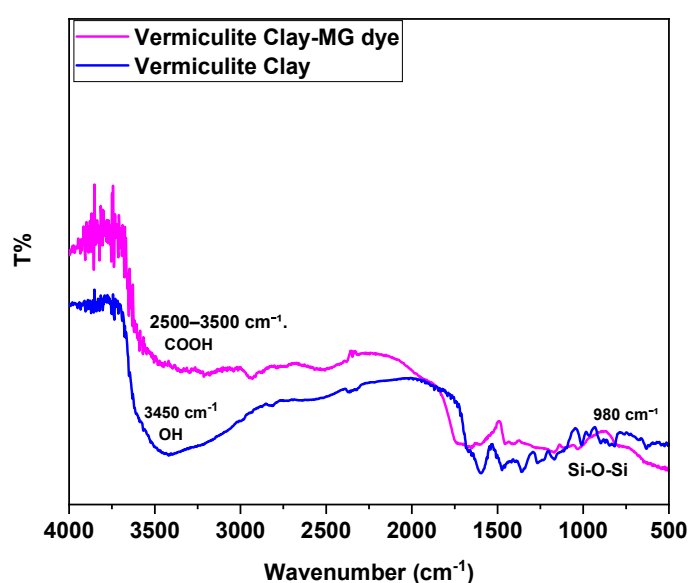


Fig. 5. FTIR of Clay and Clay after adsorption

Thermogravimetric Analysis (TGA). The TGA was conducted to evaluate the clay sample's thermal stability and decomposition behavior, as illustrated in Fig. 6. The TGA curve shows a single main weight loss event occurring in distinct temperature ranges, reflecting different stages of thermal degradation. The initial weight loss in the temperature range of approximately 10°C to 400°C is primarily attributed to the evaporation of physically adsorbed water and moisture content from the clay surface and interlayers. This stage indicates the presence of hygroscopic water commonly retained within the clay structure. A second weight loss is observed between 400°C and 600°C , corresponding to the decomposition of organic components and functional groups. This stage is primarily associated with the decarboxylation process and the release of carbon dioxide (CO_2) gas. During this stage, the loss of carboxyl and other labile groups further reflects structural changes and thermal degradation of any organic matter present within or bound to the clay matrix. Overall, the TGA results confirm the thermal behaviour of the clay, showing initial dehydration followed by decomposition of functional groups at elevated temperatures [19].

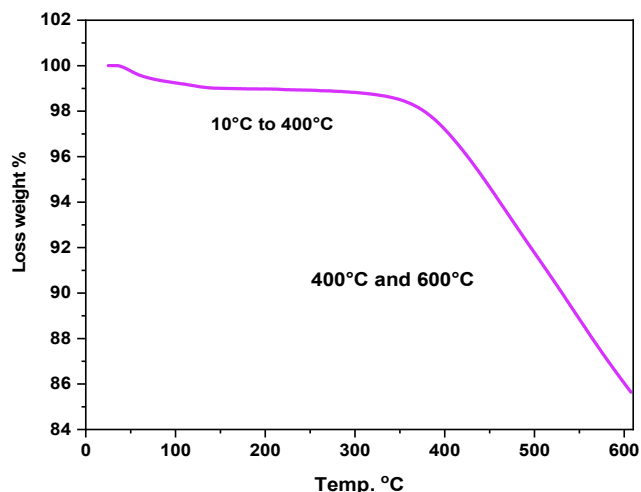


Fig. 6. Thermogravimetric Analysis (TGA) of Clay

pH Solution. Dye adsorption depends on the surface properties of the adsorbent and the distribution of the MG dye within the solution and is primarily affected by the pH level of the system. In this study, the pH ranged from 2 to 11. Fig. 7 illustrates the effect of pH on the dye adsorption using clay. The results showed that the dye removal percentage using clay decreased steadily with increasing pH, reaching a maximum value of 99.62%. Furthermore, the maximum adsorption capacity achieved was 79.77 mg/g. At pH levels greater than 7, the dye adsorption was lower. The removal percentage recorded at pH 11 was 30.33% for clay, with a corresponding maximum adsorption capacity of 24.44 mg/g. Higher pH leads to a decrease in hydrogen ion (H^+) concentration, which reduces the competition between dye ions and protons for adsorption sites on the particle surface. In addition, higher pH promotes the precipitation of dye ions from the solution as hydroxides, another factor that may enhance dye ion adsorption. The formation of soluble hydroxyl complexes causes a decrease in adsorption, which is observed at pH levels above 7 [20].

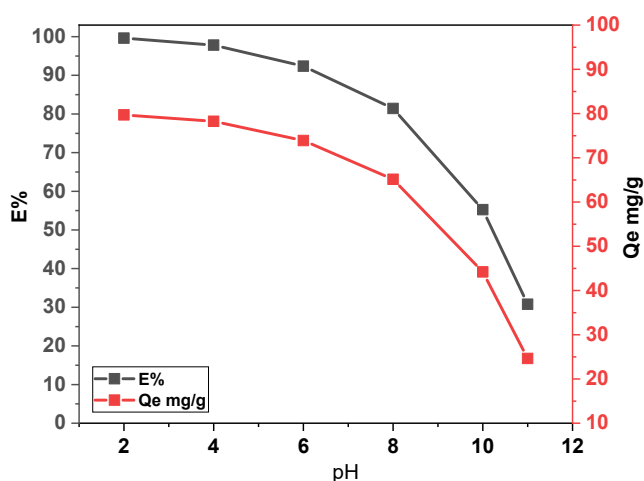


Fig. 7. Effect of pH solution on the removal of MG dye

Adsorption dosage. The importance of adsorbent dosage lies in its direct impact on adsorption efficiency. Changing the amount of adsorbent alters its ability to capture substances from the solution, thus impacting the overall efficiency of the process. In this study, the effect of clay dosage on adsorption ranged from 0.05 to 0.2 g intervals. Fig. 8 illustrates the effect of adsorbent dosage on clay dye removal. Based on the graph, the figure shows a clear trend where the dye removal rate reaches its optimum at a dosage of 0.1 g of adsorbent. The limited number of

adsorbent types explains this optimum point. Furthermore, it is logical to assume that increasing the adsorbent dosage may increase the availability of exchange sites for dye ions. Maximum dye removal was achieved using clay at a concentration of 80 mg/g, with an average removal efficiency of 92.08%. Additionally, the maximum adsorption capacity reached 73.86 mg/g. However, no increase in removal rate was observed after 0.1 g. These results may be attributed to overlapping adsorption sites resulting from the crowding of sorbent molecules. Furthermore, this shift indicates a potential saturation point or optimum dosage, indicating that beyond this point, further increases in sorbent dosage do not proportionally enhance removal efficiency, resulting in a decrease in removal ratio [21, 22].

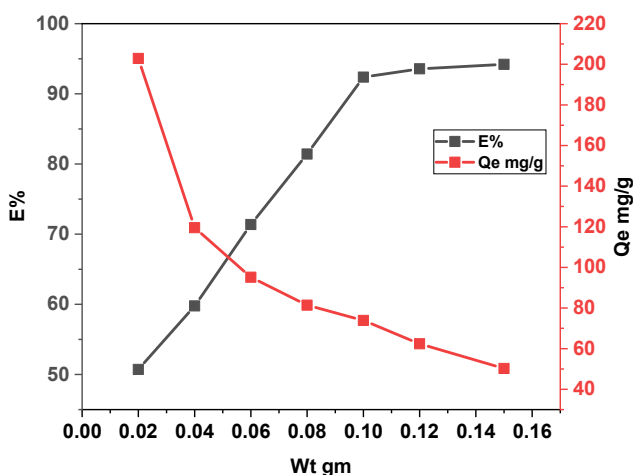


Fig. 8. Effect of the weight of clay on the removal of MG dye

Effect of initial concentration. The degree of adsorption of an adsorbate solution depends on its initial concentration. As depicted in Fig. 9, the extent of adsorption on Clay increases with increased concentrations of MG in the external solution. MG’s Qe mg/g values were identified as 89.88 mg/g for Clay. The adsorption phenomenon becomes more pronounced as the adsorbate concentration increases. The driving force behind this escalation is the elevated concentration of solute in the system. The obstacle to mass transfer between the solid adsorbent and the liquid phase is overcome by this increased solute concentration, which functions as a powerful force for diffusion. The rise in adsorbate concentration creates favorable conditions for adsorption, facilitating effective interaction between the adsorbate molecules and the adsorption sites on the adsorbent [23].

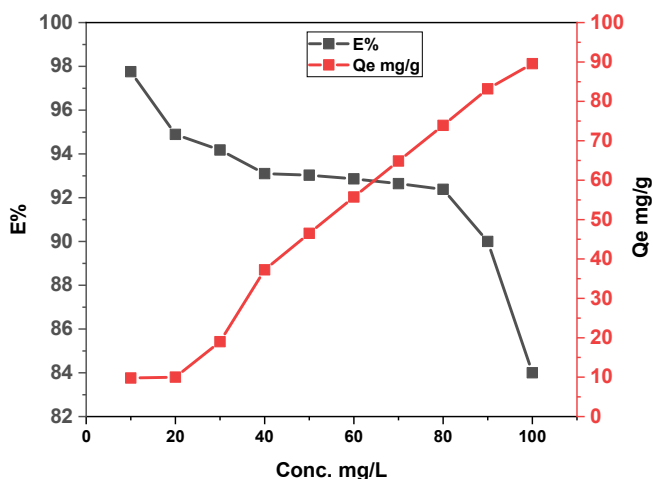


Fig. 9. Effect of initial concentration of MG dye by clay nano

Contact Time. Fig. 10 shows the adsorption efficiency curves of the clay concerning MG dye at concentrations of 100 ml/L. The results indicate that the adsorption capacity of the clay increased rapidly during the first 15 minutes, reaching saturation at 1 hour, with a final removal efficiency of 93.22%. Notably, no significant change in the adsorption capacity was observed when the contact time was extended beyond 60 minutes. In subsequent experiments, a saturation adsorption time of 1 hour was chosen to ensure that the adsorption equilibrium state was reached while maintaining a reasonable time. Sufficient active sites are available for the dye species to adhere to at low concentrations. However, as the initial dye concentration increases, active sites become insufficient for effective adsorption [24].

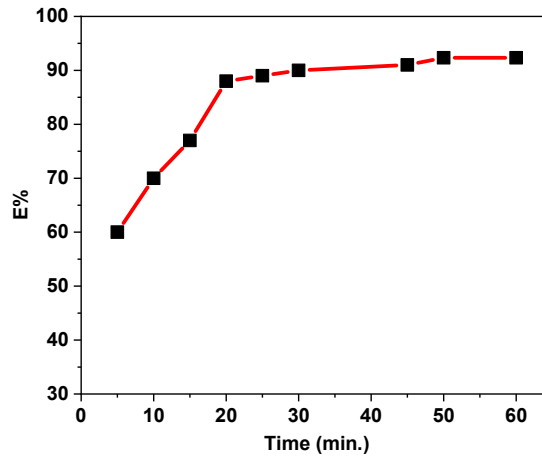


Fig. 10. Effect of equilibrium time of MG dye by using Clay

Thermodynamic Studies. To evaluate the thermodynamic nature of the adsorption process—whether endothermic or exothermic—adsorption isotherms were studied at various temperatures (10–40 °C) using an initial MG dye concentration of 50 mg·L⁻¹. The results revealed that the equilibrium adsorption capacity increased with rising temperature, indicating that the process is endothermic. This enhancement can be attributed to increased mobility of dye molecules, reduced viscosity of the solution, and improved diffusion through the external surface and internal pores of the adsorbent. Higher temperatures may also promote pore expansion, further facilitating dye uptake. These observations highlight the importance of temperature as a crucial parameter in adsorption. Furthermore, the data enabled the calculation of thermodynamic parameters such as Gibbs free energy change (ΔG), enthalpy change (ΔH), and entropy change (ΔS), using the adsorption equilibrium constant (K_e) determined at each temperature, as outlined in Equations (3-6) [25].

$$K_e = \frac{(Q_{max}) * Wt (gm)}{(C_e) * V(L)} \times 1000 \quad (3)$$

$$\Delta G = -RT \ln K_e \quad (4)$$

$$\Delta G = \Delta H - T\Delta S \quad (5)$$

$$\ln X_m = -\frac{\Delta H^\circ}{RT} + Cons. \quad (6)$$

The thermodynamic parameters ΔH and ΔS were calculated from the slope and intercept of the Van't Hoff plot of $\ln X_m$ versus $1/T$, as shown in Fig. 11. The corresponding values are summarised in Table 1. The positive ΔH confirms that the adsorption of MG dye onto the adsorbent is endothermic. The negative values of ΔG at all studied temperatures indicate that the process is spontaneous and thermodynamically favourable. The large positive ΔS reflects an increase in randomness at the solid–liquid interface during adsorption. This can be attributed to the displacement of structured dye ions near the adsorbent surface into a more disordered state upon adsorption, resulting in enhanced rotational and translational freedom of the system.

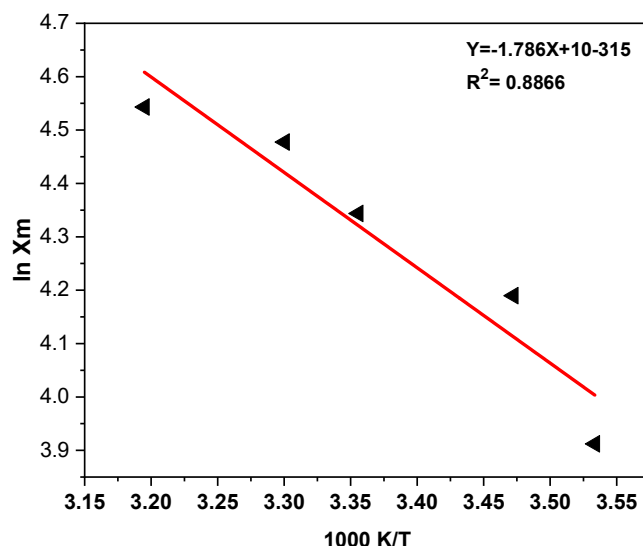


Fig. 11. Plot $\ln X_m$ against the absolute temperature of the adsorption (MG dye) onto nanoclay

Table 1. Thermodynamic Factors for MG adsorption on nanoclay

Nanoclay			
ΔH° (KJ/mol)	ΔG° (kJ/mol)	ΔS° (J.mol ⁻¹ .K ⁻¹)	Equilibrium constant
14.875	-6297.56	85.876	14.53488
	-7196.4		19.18605
	-7830.33		22.38372

Regeneration and Reusability of Nanoclay. The regeneration capacity of the nanoclay adsorbent was systematically evaluated over six consecutive adsorption-desorption cycles using ethanol and distilled water as desorbing agents. The results demonstrated that the nanoclay maintained high adsorption efficiency throughout the cycles, with only a slight decline observed in the final cycle. After the sixth cycle, the adsorbent retained approximately 93.33–80% of its original dye removal capacity, indicating excellent structural stability and surface integrity (Fig. 12). This high level of reusability is attributed to the robustness of the clay's multilayered porous structure, which remained largely intact despite repeated adsorption and desorption processes.

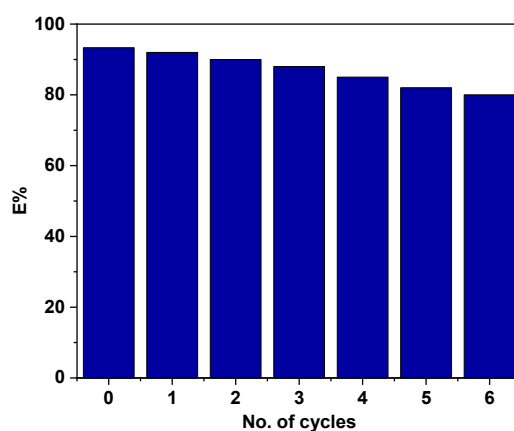


Fig. 12. The regeneration capacity of the nanoclay

FTIR spectra collected after each cycle confirmed the preservation of key functional groups, including hydroxyl and silicate moieties, which are responsible for dye binding. The minimal shift

in characteristic peaks suggested that the interaction between the MG dye and nanoclay remained largely reversible, enabling effective regeneration. Furthermore, FESEM images revealed negligible morphological degradation or pore collapse across the cycles, supporting the conclusion that the physical structure of the nanoclay was not significantly compromised. The gradual decrease in efficiency is likely due to minor residual dye accumulation or partial blockage of active sites that were not completely regenerated during the desorption process. Overall, these findings confirm the nanoclay's potential as a reusable and sustainable adsorbent for treating dye-contaminated wastewater, with strong performance maintained across multiple regeneration cycles [2, 26].

Ionic strength. Fig. 13 illustrates the effect of ionic strength on the adsorption capacity of MG dye. An apparent decrease in adsorption was observed with the addition of salts, which can be attributed to the competitive interaction between the positively charged MG dye molecules and the cations from the salts for the active adsorption sites. The presence of electrolytes in the solution leads to partial neutralization of the adsorbent surface charge and hinders the electrostatic attraction between the dye and the adsorbent. As the ionic strength increases, the screening effect becomes more pronounced, effectively reducing the availability of active sites for dye adsorption. Additionally, the presence of salts may enhance the solubility of MG dye in the aqueous medium, further decreasing its tendency to adsorb onto the surface. This experiment highlights the significant role of ionic strength in adsorption processes, as it directly influences the interaction forces between the adsorbate and the adsorbent, which is crucial for optimizing treatment conditions in real wastewater systems where ionic content is typically high [27, 28].

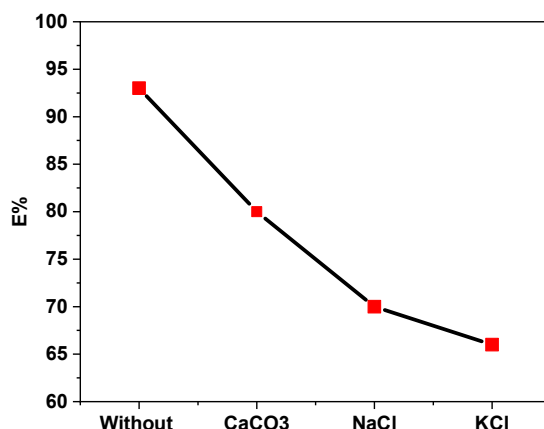


Fig. 13. Effect of ionic strength on the adsorption of MG dye on nanoclay

Adsorption Isotherms. The Freundlich isotherm is defined through the following equation 7 [29].

$$q_e = K_f C_e^{\frac{1}{n}} \quad (7)$$

q_e represents the amount of adsorbate adsorbed per unit mass of adsorbent at equilibrium and is typically expressed in mg/g or mol/g. C_e denotes the equilibrium concentration of the adsorbate remaining in solution after the adsorption process, given in mg/L or mol/L. K_f is the empirical Freundlich constant, also known as the capacity factor, which indicates the adsorption capacity of the adsorbent and is expressed in $(\text{mg/g})(\text{L/mg})^{1/n}$. The term $1/n$ is the Freundlich intensity parameter. If the value of n equals 1, the adsorption process is linear, suggesting homogenous surface energies. A value of n less than 1 indicates a chemical adsorption process, whereas a value greater than 1 suggests a physical adsorption mechanism is dominant [30, 31].

Langmuir Isotherm. The Langmuir model is mostly utilized for dye adsorption from liquid solutions. The nature of the adsorption process was derived by Langmuir's alternative equation 8 [32]:

$$q_e = \frac{q_m K_L C_e}{1 + K_L C_e} \quad (8)$$

q_e is amount adsorbed per unit weight of adsorbent at equilibrium (mg/g); C_e is equilibrium concentration of adsorbent in solution after adsorption (mg/L); q_m is Empirical Langmuir constant which represents maximum adsorption capacity (mg/g) of the total number of surface sites per mass of adsorbent and it may vary among different compounds because of differences in adsorbate sizes; K_L is empirical Langmuir constant (L/mg) or the equilibrium constant of the adsorption reaction [33].

The coefficients of determination (R^2) and isotherm parameters from the nonlinear regression method are listed in Table 2. A comparison of nonlinearly fitted curves from experimental data at 30 °C is shown in Fig. 14. A plot of q_e vs C_e (Figure 14) where the values of K_F and $1/n$ are obtained from the intercept and slope of the linear regressions (Table 2). The correlation coefficient, R^2 values for the Langmuir and Freundlich models at temperature (30 °C) are (0.9988) and (0.9729) for nanoclay [34, 35].

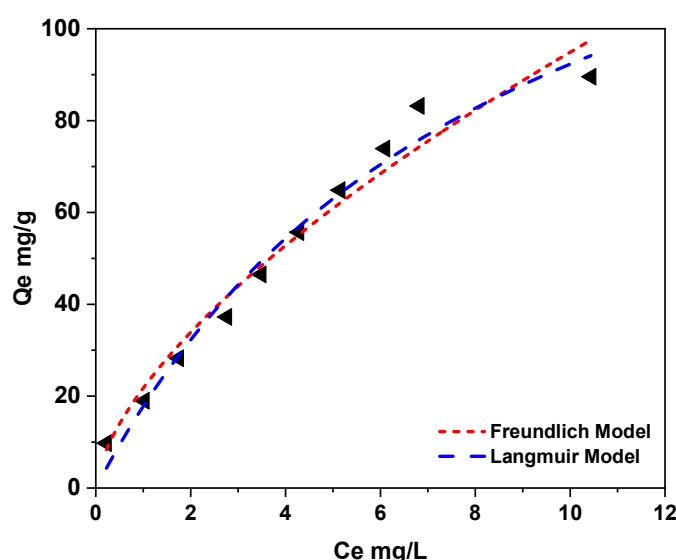


Fig. 14. Adsorption isotherm models nonlinear fit of adsorption of MG dye onto nanoclay

Table 2. Different Factors of models for the adsorption study of MG dye onto nanoclay

Nanoclay		
Temperature/ °C		30 °C
Freundlich Isotherm	K_f	30.11 ± 0.544
	$1/n$	0.344 ± 0.011
	R^2	0.9988
Langmuir Isotherm	q_m (mg/g)	85.936 ± 12.22
	K_L (L/mg)	0.344 ± 0.022
	R^2	0.9729

Adsorption kinetics. The study of adsorption kinetics is crucial, as it provides insights into both the adsorption rate—a key factor in evaluating the efficiency of an adsorbent—and the underlying mechanism of the adsorption process. Fig. 15 illustrates the variation of the amount of MG dye adsorbed (q_t) over time. The adsorption rate is notably high during the initial stages, with the majority of dye uptake occurring within the first 10 minutes. This rapid initial adsorption suggests that nanoclay exhibits a strong affinity for MG dye and possesses a high adsorption rate.

To analyze the adsorption kinetics of MG dye by nanoclay the pseudo-first-order [36], pseudo-second-order [37], were tested. The result of the fitting is listed in Table 3. A simple kinetic analysis of adsorption (pseudo-first-order equation) is in the form:

$$q_t = q_e [1 - \exp(-k_f t)] \quad (9)$$

Where q_t is the amount of adsorbate adsorbed at time t (mg/g), q_e is the adsorption capacity in the equilibrium (mg/g), k_f is the pseudo-first-order rate constant (min^{-1}), and t is the contact time (minutes).

A pseudo-second-order equation based on adsorption equilibrium capacity may be expressed in the form:

$$q_t = \frac{K_2 q_e t}{1 + K_2 q_e t} \quad (10)$$

Where K_2 is the pseudo-second-order rate constant ($\text{g} \cdot \text{mg}^{-1} \cdot \text{min}^{-1}$), the initial sorption rate (expressed in $\text{mg} \cdot \text{g}^{-1} \cdot \text{min}^{-1}$) can be obtained when t approaches zero, equation (11).

$$h = k_2 q_e^2 \quad (11)$$

Fig. 15 illustrates the effect of contact time (0–60 minutes) on the adsorption of MG dye onto nanoclay at an initial dye concentration of $50 \text{ mg} \cdot \text{L}^{-1}$. The figure reveals that dye adsorption proceeds rapidly during the initial stage, followed by a gradual decrease in the adsorption rate as the system approaches equilibrium. This initial rapid uptake can be attributed to the abundance of available active sites on the nanoclay's surface. Over time, as these sites become occupied, the rate slows until equilibrium is reached. Kinetic analysis of the experimental data showed a better fit to the pseudo-second-order model, as evidenced by higher correlation coefficient (R^2) values. Furthermore, the calculated adsorption capacities (q_e, cal) from the pseudo-second-order model were more consistent with the experimentally observed values (q_e, exp) compared to those derived from the pseudo-first-order model, suggesting that the adsorption of MG dye onto nanoclay is predominantly governed by physisorption mechanisms [38-40].

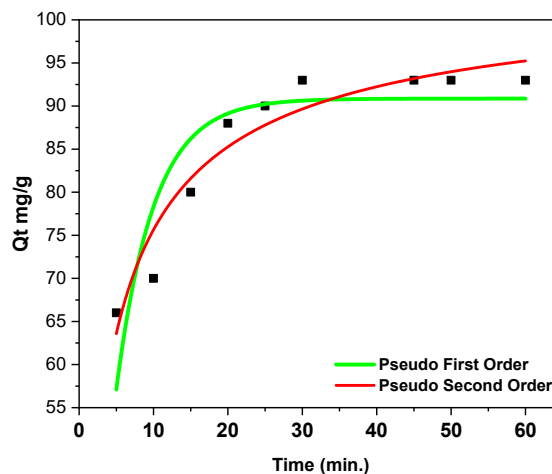


Fig. 15. Nonlinear adsorption kinetics model fit for adsorption of MG dye onto nanoclay

Table 3. Kinetic constants and correlation coefficients for MG dye adsorption onto nanoclay

Parameters	Value	Stand. Error	R^2
Pseudo first-order			
Q_e ($\text{mg} \cdot \text{g}^{-1}$)	90.99	± 2.333	0.766

K_1 (min^{-1})	0.133	± 0.0433	
pseudo-second-order			
Q_e ($\text{mg}\cdot\text{g}^{-1}$)	104.44	± 3.898	0.9033
K_2 ($\text{gm}\cdot\text{g}^{-1}\cdot\text{min}^{-1}$)	0.44	± 0.266	
h_0 ($\text{mg}\cdot\text{g}^{-1}\cdot\text{min}^{-1}$)	$4.7*10^6$		

Conclusion

Adsorbent for the removal of malachite green (MG) dye from aqueous solutions. Comprehensive material characterization using XRD, FESEM, TEM, TGA, and FTIR confirmed that the nanoclay possesses a multilayered, porous structure favorable for adsorption. Batch experiments identified the optimal conditions as 0.05 g of adsorbent dosage, pH 7, a dye concentration of 30 mg/L, a contact time of 60 minutes, and a temperature of 30°C, achieving a maximum removal efficiency of 93.84%. FTIR analysis confirmed the interaction between MG dye molecules and functional groups on the nanoclay surface, while FESEM and TEM images revealed morphological changes and surface interactions following adsorption. Additionally, adsorption isotherms, kinetic models, and thermodynamic parameters were thoroughly investigated. The adsorption process followed the Freundlich isotherm and pseudo-second-order kinetics, while thermodynamic analysis confirmed the endothermic and spontaneous nature of the process. Notably, the nanoclay exhibited excellent reusability, retaining over 90% of its adsorption capacity after five regeneration cycles using ethanol and water, emphasizing its structural stability and potential for practical wastewater treatment applications.

References

1. Ullah N., Ali Z., Khan A.S., Adalat B., Nasrullah A., Khan Sh.B. Preparation and dye adsorption properties of activated carbon/clay/sodium alginate composite hydrogel membranes. *RSC Advances*, 2024, **Vol. 14(1)**, p. 211-221. DOI: [10.1039/D3RA07554K](https://doi.org/10.1039/D3RA07554K)
2. Thamer B.M., Shaker A.A., Abdul Hameed M.M., Al-Enizi A.M. Highly selective and reusable nanoadsorbent based on expansive clay-incorporated polymeric nanofibers for cationic dye adsorption in single and binary systems. *Journal of Water Process Engineering*, 2023, **Vol. 54**, 103918. DOI: [10.1016/j.jwpe.2023.103918](https://doi.org/10.1016/j.jwpe.2023.103918).
3. Shah L.A., Subhan H., Alam S., Ye D., Ullah M. Bentonite clay reinforced alginate grafted composite hydrogel with remarkable sorptive performance toward removal of methylene green. *International Journal of Biological Macromolecules*, 2024, **Vol. 279**, 135600. DOI: [10.1016/j.ijbiomac.2024.135600](https://doi.org/10.1016/j.ijbiomac.2024.135600)
4. Chien S., Clayton W. Application of Elovich equation to the kinetics of phosphate release and sorption in soils. *Soil Science Society of America Journal*, 1980, **Vol. 44(2)**, p. 265-268. DOI: [10.2136/sssaj1980.03615995004400020013x](https://doi.org/10.2136/sssaj1980.03615995004400020013x)
5. Aljeboree A.M., Alkaim A.F., Alsultany F.H., Issa S.K. Highly Reusable Nano Adsorbent Based on Clay-Incorporated Hydrogel Nanocomposite for Cationic Dye Adsorption. *Journal of Inorganic and Organometallic Polymers and Materials*, 2024, **Vol. 35**, p. 1165-1180. DOI: [10.1007/s10904-024-03344-5](https://doi.org/10.1007/s10904-024-03344-5).
6. Kumari P., Kaushal D., Chauhan V., Shandilya P., Kumar M. Synthesis of gum acacia-cl-acrylic acid-co-itaconic acid hydrogels for efficient removal of toxic dye rhodamine-B: A step for sustainable environment. *International Journal of Biological Macromolecules*, 2025, **Vol. 292**, 139296. DOI: [10.1016/j.ijbiomac.2024.139296](https://doi.org/10.1016/j.ijbiomac.2024.139296).
7. Al-Aidy H., Amdeha E. Green adsorbents based on polyacrylic acid-acrylamide grafted starch hydrogels: the new approach for enhanced adsorption of malachite green dye from aqueous solution. *International Journal of Environmental Analytical Chemistry*, 2021, **Vol. 101(15)**, p. 2796-2816. DOI: [10.1080/03067319.2020.1711896](https://doi.org/10.1080/03067319.2020.1711896).

8. Rahul, Jindal R. Efficient removal of toxic dyes malachite green and fuchsin acid from aqueous solutions using Pullulan/CMC hydrogel. *Polymer*, 2024, **Vol. 307**, 127203. DOI: [10.1016/j.polymer.2024.127203](https://doi.org/10.1016/j.polymer.2024.127203).
9. Tyagi R., Dangi D., Sharma P. Optimization of Hazardous Malachite Green Dye Removal Process Using Double Derivatized Guar Gum Polymer: A Fractional Factorial L9 Approach. *Sustainable Chemistry for Climate Action*, 2024, **Vol. 100043**. DOI: [10.1016/j.scca.2024.100043](https://doi.org/10.1016/j.scca.2024.100043).
10. García-Guzmán P., Medina-Torres L., Bernad-Bernad M.J., Calderas F., Manero O. Study of the cholesterol adsorption and characterization of montmorillonite and bentonite clay. *Materials Today Communications*, 2023, **Vol. 35**, 105604. DOI: [10.1016/j.mtcomm.2023.105604](https://doi.org/10.1016/j.mtcomm.2023.105604).
11. Abu Elella M.H., Aamer N., Abdallah H.M., López-Maldonado E.A., Mohamed Y.M.A., El Nazer H.A., Mohamed R.R. Novel high-efficient adsorbent based on modified gelatin/montmorillonite nanocomposite for removal of malachite green dye. *Scientific Reports*, 2024, **Vol. 14(1)**, 1228. DOI: [10.1038/s41598-024-51321-2](https://doi.org/10.1038/s41598-024-51321-2)
12. Himashi, Lal B., Suman, Lakshmaiya N., Ahmed J., Alshehri S.M., Singh P.T., Singh S., Kandwal A., Jasrotia R. Insights into the microstructural, optical and magnetic characteristics of cobalt and dysprosium co-doped BaFe₁₂O₁₉ M-type hexagonal ferrites. *Journal of Sol-Gel Science and Technology*, 2025, **Vol. 114**, p. 581-593. DOI: [10.1007/s10971-025-06705-9](https://doi.org/10.1007/s10971-025-06705-9).
13. Ahmad Ramli S., Zin R.M., Ahmad M.K., Azyan N.I., Hamed N.K.A., Saputri D.G., Nurhaziqah A.M.S., Nafarizal N., Silambarasan K., Suriani A.B., Ahmad M.Y. MoS₂-decorated etched-TiO₂ rods film for superior photocatalytic dye degradation. *Journal of Sol-Gel Science and Technology*, 2025, **Vol. 114**, p. 641-659. DOI: [10.1007/s10971-025-06702-y](https://doi.org/10.1007/s10971-025-06702-y).
14. Alkaim A.F., Hussein F.H. Photocatalytic degradation of edta by using TiO₂ suspension. *International Journal of Chemical Sciences*, 2012, **Vol. 10(1)**, p. 586-598.
15. Borah M., Konwar U., Gogoi P., Boruah P., Bora J.G., Garg S., Ahmed T.H. Das B. Decolorization of tea industry wastewater utilizing tea waste bio-adsorbent in fixed-bed adsorption column: breakthrough curves analysis and modeling. *Sustainable Water Resources Management*, 2024, **Vol. 10**, 37. DOI: [10.1007/s40899-023-01020-z](https://doi.org/10.1007/s40899-023-01020-z)
16. Ahmad R. Studies on adsorption of crystal violet dye from aqueous solution onto coniferous pinus bark powder (CPBP). *Journal of Hazardous Materials*, 2009, **Vol. 171(1)**, p. 767-773. DOI: [10.1016/j.jhazmat.2009.06.060](https://doi.org/10.1016/j.jhazmat.2009.06.060).
17. Bader A.T., Aljeboree A.M., Alkaim A.F. Removal of Methyl Violet (MV) from aqueous solutions by adsorption using activated carbon from pine husks (plant waste sources). *Plant Archives*, 2019, **Vol. 19**, p. 898-901.
18. Subhan H., Alam S., Shah L.A., Ali M.W., Farooq M. Sodium alginate grafted poly(N-vinyl formamide-co-acrylic acid)-bentonite clay hybrid hydrogel for sorptive removal of methylene green from wastewater. *Colloids and Surfaces A: Physicochemical and Engineering Aspects*, 2021, **Vol. 611**, 125853. DOI: [10.1016/j.colsurfa.2020.125853](https://doi.org/10.1016/j.colsurfa.2020.125853).
19. Aljeboree A.M., Alkaim A.F., Hussein Sh.A., Alsultany F.H., Jawad M.A. Ecofriendly k-Carrageenan-Based Hydrogel with Strong Adsorption and Higher Abilities to Remove Crystal Violet from Aqueous Solution: Thermodynamic, Isotherm and Kinetic Investigation. *Journal of Inorganic and Organometallic Polymers and Materials*, 2024, **Vol. 35**, p. 2921-2942. DOI: [10.1007/s10904-024-03434-4](https://doi.org/10.1007/s10904-024-03434-4).
20. Parveen R., Tarannum Z., Ali Sh., Fatima S. Nanoclay based study on protein stability and aggregation and its implication in human health. *International Journal of Biological Macromolecules*, 2021, **Vol. 166**, p. 385-400. DOI: [10.1016/j.ijbiomac.2020.10.197](https://doi.org/10.1016/j.ijbiomac.2020.10.197).
21. Aljeboree A.M., Hasan I.T., Al-Warthan A., Alkaim A.F. Preparation of sodium alginate-based SA-g-poly(ITA-co-VBS)/RC hydrogel nanocomposites: And their application towards dye adsorption. *Arabian Journal of Chemistry*, 2024, **Vol. 17(3)**, 105589. DOI: [10.1016/j.arabjc.2023.105589](https://doi.org/10.1016/j.arabjc.2023.105589)
22. Lebkiri I., Abbou B., Kadiri L., Ouass A., Elamri A., Ouaddari H., Elkhatabi O., Lebkiri A., Rifil E.H. Swelling properties and basic dye adsorption studies of polyacrylamide

- hydrogel. *Desalination and Water Treatment*, 2021, **Vol. 233**, p. 361-376. DOI: [10.5004/dwt.2021.27530](https://doi.org/10.5004/dwt.2021.27530).
23. Vieira T., Artifon S.E.S., Cesco C.T., Vilela P.B., Becegato V.A., Paulino A.T. Chitosan-based hydrogels for the sorption of metals and dyes in water: isothermal, kinetic, and thermodynamic evaluations. *Colloid and Polymer Science*, 2021, **Vol. 299**, p. 649–662. DOI: [10.1007/s00396-020-04786-2](https://doi.org/10.1007/s00396-020-04786-2)
 24. Mubarik S., Ehsan S., Imran M., Hanif F. Linear and nonlinear modeling of kinetics and isotherms characterizing adsorptive removal of 4-nitrophenol by biochar BC-PFP773. *Desalination and Water Treatment*, 2022, **Vol. 250**, p. 240-251. DOI: [10.5004/dwt.2022.28246](https://doi.org/10.5004/dwt.2022.28246).
 25. Soubai B., Chham A., Selhami B., Akouibaa M., Ali S.A.S., El foulani A.A., Tahiri M. Transforming animal waste into a friendly and economically sustainable adsorbent for removing organic pollutants from aqueous wastewater. *Case Studies in Chemical and Environmental Engineering*, 2024, **Vol. 10**, 100981. DOI: [10.1016/j.cscee.2024.100981](https://doi.org/10.1016/j.cscee.2024.100981).
 26. Abdulhameed A.S., Jawad A.H., Mohammad A.-T. Synthesis of chitosan-ethylene glycol diglycidyl ether/TiO₂ nanoparticles for adsorption of reactive orange 16 dye using a response surface methodology approach. *Bioresource Technology*, 2019, **Vol. 293**, 122071. DOI: [10.1016/j.biortech.2019.122071](https://doi.org/10.1016/j.biortech.2019.122071).
 27. Abdulsahib W.K., Ganduh S.H., Radia N.D., Jasim L.S. New Approach for Sulfadiazine Toxicity Management using Carboxymethyl Cellulose Grafted Acrylamide Hydrogel. *International Journal of Drug Delivery Technology*, 2020, **Vol. 10(2)**, p. 259-264.
 28. Abdulsahib W.K., Ganduh S.H., Mahdi M.A., Jasim L.S. Adsorptive removal of doxycycline from aqueous solution using graphene oxide/hydrogel composite. *International Journal of Applied Pharmaceutics*, 2020, **Vol. 12(6)**, p. 100-106.
 29. Freundlich H.W. The Adsorption of cis- and trans-Azobenzene. *J Am Chem Soc*, 1939, **Vol. 61**, p. 2228-2230.
 30. Liu Y., Chen Y., Shi Y., Wan D., Chen J., Xiao Sh. Adsorption of toxic dye Eosin Y from aqueous solution by clay/carbon composite derived from spent bleaching earth. *Journal of Hazardous Materials*, 2019, **Vol. 93(1)**, p. 4656-5544. DOI: [10.1002/wer.1376](https://doi.org/10.1002/wer.1376)
 31. Kim Y.-S., Kim J.-H. Isotherm, kinetic and thermodynamic studies on the adsorption of paclitaxel onto Sylopute. *The Journal of Chemical Thermodynamics*, 2019, **Vol. 130**, p. 104-113. DOI: [10.1016/j.jct.2018.10.005](https://doi.org/10.1016/j.jct.2018.10.005)
 32. Langmuir I. The adsorption of gases on plane surfaces of glass, mica and platinum. *Journal of the American Chemical society*, 1918, **Vol. 40(9)**, p. 1361-1403. DOI: [10.1021/ja02242a004](https://doi.org/10.1021/ja02242a004)
 33. Zaheer Z., Al-Asfar A., Aazam E.S. Adsorption of methyl red on biogenic Ag@Fe nanocomposite adsorbent: Isotherms, kinetics and mechanisms. *Journal of Molecular Liquids*, 2019, **Vol. 283**, p. 287-298. DOI: [10.1016/j.molliq.2019.03.030](https://doi.org/10.1016/j.molliq.2019.03.030)
 34. Siva Kumar N., Asif M., Poulouse A.M., Suguna M., Al-Hazza M.I. Equilibrium and Kinetic Studies of Biosorptive Removal of 2,4,6-Trichlorophenol from Aqueous Solutions Using Untreated Agro-Waste Pine Cone Biomass. *Processes*, 2019, **Vol. 10(7)**, 757. DOI: [10.3390/pr7100757](https://doi.org/10.3390/pr7100757)
 35. Alipanahpour Dil E., Ghaedi M., Ghaedi A.M., Asfaram A., Goudarzi A., Hajati S., Soylak M., Agarwal Sh., Gupta V.K. Modeling of quaternary dyes adsorption onto ZnO-NR-AC artificial 3 neural network: Analysis by derivative spectrophotometry. *Journal of Industrial and Engineering Chemistry*, 2016, **Vol. 34**, p. 186-197. DOI: [10.1016/j.jiec.2015.11.010](https://doi.org/10.1016/j.jiec.2015.11.010)
 36. Lagergren S. About the theory of so-called adsorption of soluble substances. *Kunliga Suensk Vetenskapsakademiens Handlingar*, 1898, **Vol. 241**, p. 1-39.
 37. Ho Y.S., McKay G. Pseudo-second order model for sorption processes. *Process Biochem.*, 1999, **Vol. 34(5)**, p. 451-465. DOI: [10.1016/S0032-9592\(98\)00112-5](https://doi.org/10.1016/S0032-9592(98)00112-5)
 38. Kamran U., Heo Y.-J., Lee J.W., Park S.-J. Chemically modified activated carbon decorated with MnO₂ nanocomposites for improving lithium adsorption and recovery from aqueous

- media. *Journal of Alloys and Compounds*, 2019, **Vol. 794**, p. 425-434. DOI: [10.1016/j.jallcom.2019.04.211](https://doi.org/10.1016/j.jallcom.2019.04.211)
39. Jiang R., Zhu H.-Y., Fu Y.-Q., Zong E.-M., Jiang Sh.-T., Li J.-B., Zhu J.-Q., Zhu Y.-Y., Magnetic NiFe₂O₄/MWCNTs functionalized cellulose bioadsorbent with enhanced adsorption property and rapid separation. *Carbohydrate Polymers*, 2021, **Vol. 252**, 117158. DOI:[10.1016/j.carbpol.2020.117158](https://doi.org/10.1016/j.carbpol.2020.117158)
40. Tanhaei B., Ayati A., Iakovleva E., Sillanp M. Efficient carbon interlayered magnetic chitosan adsorbent for anionic dye removal: Synthesis, characterization and adsorption study. *International Journal of Biological Macromolecules*, 2020, **Vol. 164**, p. 3621-3631. DOI: [/10.1016/j.ijbiomac.2020.08.207](https://doi.org/10.1016/j.ijbiomac.2020.08.207)